Encoding Quadrupolar Capillary Information into Saddle-Shaped Objects for Self-Assembly

Megan Delens* and Nicolas Vandewalle
GRASP, Institute of Physics B5a, University of Liège, B4000 Liège, Belgium.
(Dated: April 3, 2026)

The "Cheerios effect", which describes the capillary interaction between spherical particles at a liquid interface, has traditionally been limited to simple self-assembling structures. Our study addresses the need for more complex assemblies by exploring specific particle geometries. We introduce a theoretical model to describe the interaction potential between quadrupolar objects at the mesoscale, which reveals that both side-by-side and end-to-end long-range attractions can be achieved under specific capillary and geometrical conditions—a phenomenon we term the "Pringles effect". We experimentally validate our model's predictions by encoding this specific capillary information into 3D-printed curved ellipses, which mimic the surface geometry of Pringles crisps. This approach showcases the potential for complex self-assembling mesoscale structures through precise control over capillary-driven interactions.

I. INTRODUCTION

First proposed by Bowden et al. in 1997 [1], capillary-driven self-assembly has become a sophisticated method for constructing minuscule structures, especially useful for applications spanning microfluidics [2], microfabrication [3], drug delivery [4], and photonics [5, 6]. This technique is particularly suited for assembling structures that are too small for manual assembly yet too large for chemical synthesis, effectively bridging the gap between bottom-up and top-down fabrication methods [7–9].
The fundamental principle of capillary-driven self-assembly involves placing components at a liquid-air interface where they naturally aggregate due to capillary forces. This interaction arises from the deformation of the water surface caused by the particle's weight, which creates a gravitational well into which other particles can fall. The interaction between particles that present a flat circular contact line is either solely attractive or repulsive [10–13]. This phenomenon, often called the "Cheerios effect", refers to the way cereals aggregate in a milk bowl [12].
Using anisotropic particles rendered anisotropic by shape or wettability, it is possible to create more complex distortions. Indeed, the contact line is no longer constant but undulates along the particle sides. These distortions can thus be manipulated to create rotational movements and orientational effects in addition to attractive or repulsive interactions [14]. Such selective bonding is crucial for efficiently self-assembling complex and ordered structures [15]. Examples in nature include mosquito eggs and insects forming specific crystal-like structures [16, 17]. Specially designed tiles are also used to self-assemble into complex structures, such as Penrose tilings [18]. More recently, cross-shaped objects [19, 20] or rhombus particles [21] have been used to self-assemble into specific and reprogrammable ordered patterns. Ellipsoidal and cylindrical particles also provide complex interactions [22–25]. For these elongated particles, the end-to-end chaining, i.e., when attraction occurs along their major axis, is predominantly observed on planar interfaces for colloidal-sized particles but also higher-scaled particles [22, 23, 26]. Notably, Lewandowski et al. [26] have used interface curvature to favor side-to-side aggregation, i.e., attraction by their minor axis, of micrometer-scale cylinders, and Ershov et al. [27] demonstrated that anisotropic interface curvature can also induce spatial ordering of spherical colloids at fluid interfaces. Loudet et al. [22] have observed side-by-side attraction when changing the ellipsoids' surface chemistry. Very recently, Eatson et al. [28] demonstrated that coating ellipsoidal particles with soft polymer shells can also modulate their capillary interactions, leading to a transition from tip-to-tip to side-to-side configurations depending on the aspect ratio and shell thickness. Along similar lines, Hazra et al. [29] reported the capillary-driven self-assembly of soft ellipsoidal microgels at the air–water interface, showing that particle deformability can play a key role in determining the final arrangement of anisotropic particles.
Our goal is to enhance our understanding of capillary-driven assembly processes at the mesoscale, while also laying the foundation for designing anisotropic objects that self-assemble into predictable structures. To this end, following the capillary multipoles approach, we calculated the quadrupolar capillary interaction potential. The study of this potential and its orientational terms demonstrates how to encode multipolar components into particles to achieve either end-to-end or side-by-side configurations on a flat fluidic interface. We experimentally observe both configurations by 3D-printing curved elliptical particles, resembling Pringles crisps, with the appropriate capillary properties. Drawing an analogy to the Cheerios effect, we term the specific capillary condition that favors either configuration the "Pringles effect". Figure 1 displays top views of the liquid-air interface where these uniquely shaped Pringles self-assemble. Due to their specific geometry, they attract either in an end-to-end configuration (Figures 1(b) and (d)) or in a side-by-side configuration (Figures 1(c) and (e)), leading to the formation of different

* megan.delens@uliege.be

structures.

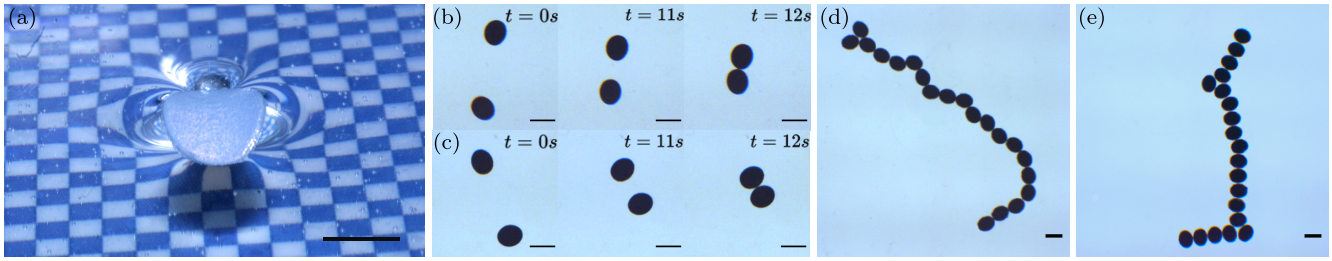

FIG. 1. **(a)** Typical 3D-printed elongated saddle-shaped objects presented in the article. When floating on the water, four lobes of deformation appear following the curvature of the object, as revealed by the refraction of a checkerboard pattern placed below. **(b)** Experimental aggregation in the end-to-end configuration of two elongated Pringles with special parameters that we call versatile Pringles. **(c)** Side-by-side aggregation with the same objects as picture (b) but flipped. **(d)** End-to-end chaining of 20 versatile Pringles. **(e)** Side-by-side chaining of the same 20 versatile Pringles as in the picture (c) but flipped. Scale bars: 5 mm.

II. MODEL FOR QUADRUPOLAR OBJECTS

The shape of the liquid interface $z(x,y)$ around a particle trapped at a fluid surface is governed by the balance between hydrostatic pressure and surface tension forces. When the interface slopes are small ($\ll 45°$), this balance is described by the linearized Young–Laplace equation [30]:

$$\rho_l g z = \gamma \nabla^2 z, \tag{1}$$

where ρ_l is the liquid density, g is the gravitational acceleration, and γ is the surface tension. This relation defines the capillary length $\lambda = \sqrt{\frac{\gamma}{\rho_l g}}$, which sets the characteristic length scale at which gravity and surface tension are balanced. For a water–air interface, this gives $\lambda = 2.7$ mm. The general solution of the Young-Laplace equation (1) gives the interface shape around a single particle with an anisotropic contact line [31–34]:

$$z(r,\theta) = \sum_{m=0}^{\infty} Q_m K_m(r/\lambda)\cos\left[m(\theta-\theta_m)\right], \tag{2}$$

where (r,θ) are cylindrical coordinates centered on the particle, Q_m is called the capillary charge of the mth order characterizing the amplitude of the deformation, K_m is the modified Bessel function of the second kind and order m, θ_m is the orientation of the mth pole. This equation can be considered as a Fourier multipole expansion, which is equivalent to summing monopole ($m = 0$), dipole ($m = 1$), quadrupole ($m = 2$), and higher-order components. Among these components, the monopolar term arises from the object's weight and scales with gravitational forces. Its amplitude is governed by the Bond number $Bo = \frac{(\rho_p - \rho_l) g a^2}{\gamma}$, where ρ_p is the particle's density and a, its characteristic size. For micron and submicron particles, $Bo \ll 1$ and the gravitational deformation is negligible [35, 36]. In this regime, capillary interactions originate primarily from the anisotropy of the contact line, with the quadrupolar term being the first non-vanishing contribution [34]. Indeed, if a particle has a dipolar moment, it would tilt when placed on the liquid surface. Hence, the dipolar component can only be considered if an external force balances this torque [35, 37, 38]. However, at the mesoscale, where $Bo \sim 1$, the gravitational contribution becomes non-negligible and monopoles are significant.

Capillary interactions between such monopolar objects can be derived using the linear superposition approximation (LSA), proposed by Nicolson [10], which assumes that the deformation induced by one object does not alter that of the other. The resulting interaction potential between monopoles is:

$$U_{ij} = -2\pi\gamma q_i q_j K_0\left(\frac{|\vec{r}_j - \vec{r}_i|}{\lambda}\right), \tag{3}$$

[33, 39, 40]. This interaction, commonly referred to as the Cheerios effect [12], is attractive or repulsive depending on the signs of the monopolar capillary charges. The Nicolson approximation holds when the separation between particles exceeds approximately twice their size [41–43].

The linear superposition approximation has also proven as useful as powerful to model the interface shape around mesoscopic complex particles by approximating higher-order deformations as superpositions of discrete capillary charges. For instance, a lattice of vertical spines piercing the interface creates a liquid profile well captured by a grid of monopolar charges [43]. Similarly, anisotropic mesoscale particles can be modeled by placing 2^m discrete charges corresponding to each multipolar mode m [20, 42, 44]. The interface elevation around such objects can therefore be modeled by:

$$z_i = \sum_{\alpha \in i} q_\alpha K_0 \left(\frac{|\vec{r} - \vec{r}_\alpha|}{\lambda} \right), \tag{4}$$

where q_α are the discrete capillary charges encoding each multipolar contribution. Extending the interaction potential of Eq. (3) under the same superposition principle, the capillary interaction between two complex-shaped particles becomes:

$$U_{ij} = -2\pi\gamma \sum_{\alpha \in i} \sum_{\beta \in j} q_\alpha q_\beta K_0 \left(\frac{|\vec{r}_\beta - \vec{r}_\alpha|}{\lambda} \right). \tag{5}$$

This discrete-charge formalism provides a versatile and physically grounded framework to model both the interface and the interactions between mesoscopic floating particles with arbitrary shapes and contact-line anisotropies. Additionally, it is worth noting that, in the limit of small charge separation, this representation is mathematically equivalent to the more traditional derivative-based multipole expansion. In particular, the quadrupolar contribution can be obtained directly from the monopolar Green's function by applying a traceless second-derivative operator, $\Phi_Q(\mathbf{r}) = Q\left(\hat{\mathbf{n}} \otimes \hat{\mathbf{n}} - \frac{1}{2}\mathbf{I}\right) : \nabla\nabla K_0\left(\frac{r}{\lambda}\right) = \frac{Q}{2\lambda^2} K_2\left(\frac{r}{\lambda}\right) \cos\left(2(\theta - \theta_0)\right)$. This connection highlights that both approaches are consistent and complementary: the derivative form makes the hierarchy of spatial decay explicit, while the discrete-charge construction offers an intuitive geometrical encoding of the particle shape.

In the present study, we focus on elongated objects whose interface deformation is well captured by the two leading orders: a central negative monopolar capillary charge q_c due to gravity, and a quadrupolar contribution arising from contact-line anisotropy, modeled as four equal discrete charges q with alternating polarity. Based on the general form of the interface elevation given by Eq. (4), the liquid profile around a particle i is given by

$$z_i = q_c K_0\left(\frac{|\vec{r}|}{\lambda}\right) - q K_0\left(\frac{|\vec{r} \pm \vec{\delta}_i|}{\lambda}\right) + q K_0\left(\frac{|\vec{r} \pm \vec{\xi}_i|}{\lambda}\right), \tag{6}$$

where $\vec{\delta}_i$ and $\vec{\xi}_i$ are vectors from the center of the object to the positions of the positive and negative quadrupolar charges, respectively. Their magnitudes are a or b, corresponding to the semi-major and semi-minor axes of the object, depending on which axis carries the positive or negative charges.
Two typical elongated quadrupolar objects separated by $\vec{r}$ are illustrated in the sketch of Figure 2. Following this schematic, one

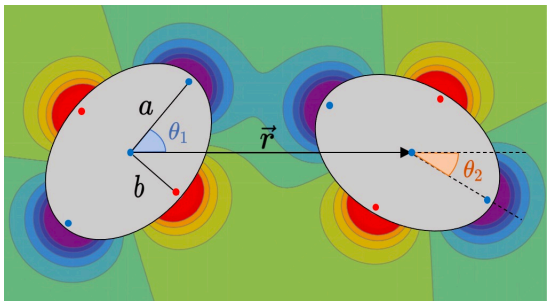

FIG. 2. Two identical elliptic quadrupolar objects at a distance r and theoretical elevation of the liquid profile around them, following Eq. (6). The colored dots inside the particles indicate negative (blue) and positive charges (red), accounting for the central monopolar charge and the four charges that comprise the quadrupole. Relative angles θ_1 and θ_2 are defined.

must consider 25 terms to calculate the interaction potential of Eq. (5) between two anisotropic floating particles. The potential is therefore described by

$$U = U_{cc} + U_{cq} + U_{qq} \tag{7}$$

where U_{cc} is the interaction potential between the two central charges, U_{cq}, the potential between a central charge and a quadrupole, and U_{qq}, the potential between the quadrupolar components. In a method analogous to our previous work [42],

we develop the Bessel functions K_0 around r with $r \gg a$ (see Appendix). This yields the elongated quadrupolar interaction potential for long and near fields as follows:

$$\begin{aligned} U &= -2\pi\gamma q_c^2 K_0\left(\frac{r}{\lambda}\right)\left[1+\frac{q}{q_c}\frac{a^2}{\lambda^2}\Theta(\theta_1,\theta_2)+\frac{q^2}{q_c^2}\frac{a^4}{\lambda^4}\Gamma(\theta_1,\theta_2)\right] \\ &= -2\pi\gamma q_c^2 K_0\left(\frac{r}{\lambda}\right)\Phi(\theta_1,\theta_2) \end{aligned} \tag{8}$$

where only leading terms are considered. Angles θ_1 and θ_2 are the angles between the axis passing through their centers and the major axis. The orientational factors are given by

$$\Gamma(\theta_1,\theta_2) = 24\left(\cos(2\theta_1)+e^2\sin^2(\theta_1)\right)\left(\cos(2\theta_2)+e^2\sin^2(\theta_2)\right) \tag{9}$$

and

$$\Theta(\theta_1,\theta_2) = \pm\left(2+\left(e^2-2\right)\left(\sin^2(\theta_1)+\sin^2(\theta_2)\right)\right), \tag{10}$$

while $\Phi(\theta_1,\theta_2)$ encodes the total orientational contribution to the interaction strength. Refer to the Appendix for a complete derivation of the potential. The form of $\Phi(\theta_1,\theta_2)$ highlights the strengthening of the attraction thanks to the quadrupolar component q compared to the monopolar interaction only. Let us discuss the preferred orientation of the particles based on their quadrupolar-monopolar ratio q/q_c, semi-major axis a, and eccentricity e of the ellipse defined as $e=\sqrt{1-b^2/a^2}$. When the quadrupole has negative charges along the major axis, $\Theta(\theta_1,\theta_2)$ is positive. The potential U is therefore minimal for orientations along the center-center axis, i.e., in four cases combining $\theta_1=\{0,\pi\}$ and $\theta_2=\{0,\pi\}$, no matter the geometrical parameters q/q_c, a and e. This configuration is generally referred to in the literature as the end-to-end configuration. It is worth noting that this orientation is perpendicular to the at-contact ground state orientation $\theta_1=\theta_2=\frac{\pi}{2}$, usually called the side-by-side configuration. The more elongated the object, the stronger the end-to-end attraction is. However, the factor $\Theta(\theta_1,\theta_2)$ changes sign when the major axis carries the positive charges. In this flipped configuration, long-range side-by-side attraction is now possible. Indeed, by comparing $\Phi(\pi/2,\pi/2)$ and $\Phi(0,0)$, we found that side-by-side attraction is favored if the conditions are such that

$$\frac{e^2a^2}{\lambda^2} < \frac{q_c}{12q}, \tag{11}$$

which corresponds to a small quadrupolar component compared to the central monopole and particles with low eccentricity. The side-by-side attraction at long distances is only possible because the central monopole has the same polarity as the minor-axis charges of the quadrupole. The Figures 3(a) and 3(b) show the contour-plot diagram of the opposite of the orientation term $\Phi(\theta_1,\theta_2)$ between (a) two particles with major axis carrying negative charges and for which the favored configuration is end-to-end, and (b) two particles with major axis carrying the positive charges and whose geometrical parameters respect the conditions of Eq. (11). One can observe that in this latter case, the side-by-side is favored. Another remark concerns the appearance of the quadrupole's dimensions in the orientation term. Indeed, the factors $(a/\lambda)^2$ and $(a/\lambda)^4$ in Eq. (8) demonstrate that the size a and b compared to the capillary length λ is highly relevant. Large objects tend to orient themselves more, while smaller objects are less sensitive to orientation effects when far from each other.

At long distances, the eccentricity e, size, and ratio $\frac{q}{q_c}$ are the key ingredients to control the dynamics and reorientation of interaction between two multipolar objects. The potential of Eq. (8) can be derived to provide radial force and torques on the objects to deduce the dynamic behavior for a pair of particles. Since the Reynolds number $Re=\frac{\rho_l\, dr/dt\; a}{\eta}\simeq 1$ is low when particles are far from each other, inertial forces can be neglected in front of dissipative forces on most parts of the trajectories of the particles. Thus, the equations of motion are:

$$\begin{aligned} -\frac{\partial U}{\partial r}+c\,\eta\, a\frac{dr}{dt} &= 0 \\ -\frac{\partial U}{\partial \theta_1}+c'\,\eta\,(ab)^{3/2}\frac{d\theta_1}{dt} &= 0 \\ -\frac{\partial U}{\partial \theta_2}+c'\,\eta\,(ab)^{3/2}\frac{d\theta_2}{dt} &= 0 \end{aligned} \tag{12}$$

with η, the dynamic viscosity; and c and c', the resistance coefficients for translation and rotation, respectively, both depending on the shape and immersion ratio.

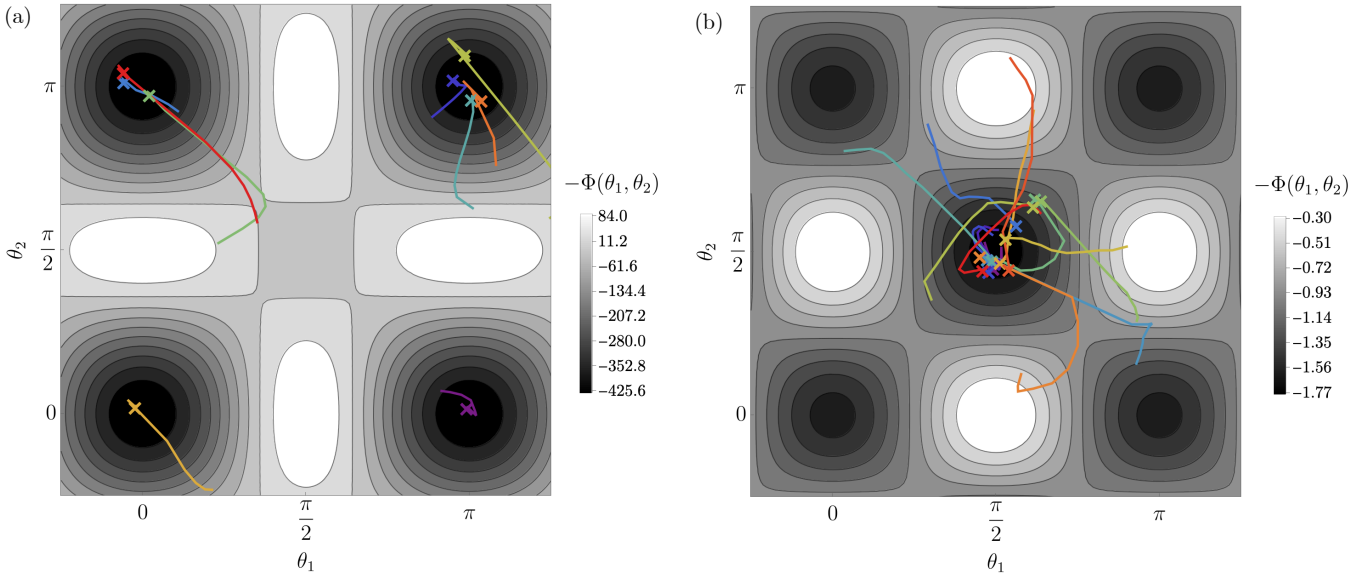

FIG. 3. **(In gray-scale)** Contour-plot diagram of the orientational term $-\Phi(\theta_1,\theta_2)$ of Eq. (8). The darkest areas correspond to the orientation (θ_1,θ_2) that minimizes the interaction potential. **(In colors)** Experimental data of the evolution of a configuration (θ_1,θ_2) of two similar objects approaching each other until contact in the configuration space θ_1,θ_2. Each color represents a different experiment. Final orientations (θ_1,θ_2) are represented by a cross $\times$. **(a)** Relative orientations favored for curved ellipses with $e = 0.87$. The four dark areas correspond to the end-to-end configuration. **(b)** Relative orientations favored for versatile Pringles ($e = 0.55$) with positive major axis. The central darkest area at ($\pi/2$,$\pi/2$) corresponds to the side-by-side configuration. The sharp orientation changes in some trajectories correspond to real transient motions occurring at the start of the experiment, caused by small residual velocities unintentionally imparted during manual placement. These motions are rapidly damped by viscous dissipation, after which capillary torque dominates and the orientation evolves smoothly.

III. EXPERIMENTAL METHODS

Elongated millimeter-scale quadrupolar objects have been designed to test our model. Using a Mathematica script, we created curved ellipses whose surface follows a hyperbolic paraboloid, like the famous Pringles crisps, and exported them as an STL file. We 3D printed the multipolar objects using a PolyJet 3D printer (Stratasys J35 Pro). This 3D-printing method boasts high precision with an announced precision of 16 μm. It prints a shell of support resin around the object that dissolves in water, ensuring the saddle curvature is precisely followed. This eliminates support structures and contact points that can alter the surface and increase roughness. Consequently, a smooth contact line is achieved, avoiding an additional capillary multipolar effect. Pictures of our typical object, focusing on edge roughness, are provided in the data supporting the article [45]. We used a resin similar to ABS plastic (Vero Blue) with a polymerized density of $\rho_p = 1180$ kg/m^3. This material is mildly hydrophilic, with a static water contact angle of approximately 50°- 60°. The positive and negative curvatures of the saddle are aligned with the minor and major axes, respectively, producing equal upward and downward deviations of the particle edges. The sharp top rim of the object promotes strong contact-line pinning, allowing us to create the desired menisci with large contact angle hysteresis [37]. Thus, the particle's deformation corresponds to the four charges that make up the quadrupole. One should note that by flipping the object upside down, the polarity of the quadrupole is therefore switched.

The previous section highlighted that three parameters are of great importance for the capillary interaction: e, a, and q/q_c. When designing our objects, each of these anisotropic aspects can be varied. The eccentricity e and the size are directly linked to the major and minor axes. The object's thickness controls the central monopole, while the quadrupolar component depends only on the parameters of the hyperbolic paraboloid. In this study, slight variations in thickness and curvature were introduced intentionally to tune the relative magnitude of the central monopolar charge q_c with respect to the quadrupolar charges q. This approach strengthens the central attraction and is essential for designing versatile objects capable of assembling either in end-to-end or in side-by-side configuration. These charges are, therefore, entirely editable when creating our multipoles, and we can measure the ratio q/q_c thanks to profilometry methods. Typically, by carefully tuning these anisotropic parameters, we have created and named three types of particles:

- Flat disks: Monopolar circular objects,
- Curved ellipses: Quadrupolar heavy objects that won't respect the conditions of Eq. (11) even if flipped,
- Versatile Pringles: Specially designed quadrupolar objects that respect the conditions of Eq. (11) to favor the side-by-side

configuration.

The three types of objects are represented in Figure 4(a,b,c). Their geometrical parameters are given in the Table I. Defining

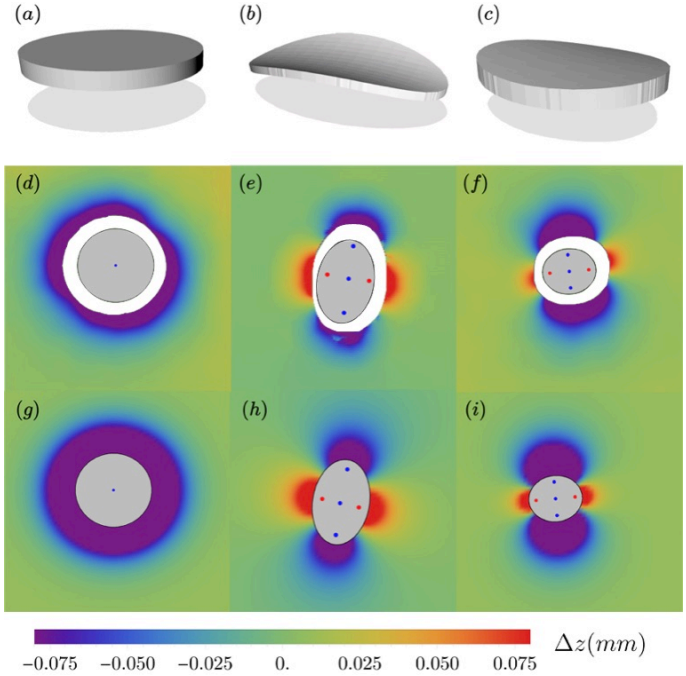

FIG. 4. **(a,b,c)** 3D view of a 3D-printed flat disk, a curved ellipse, and a versatile Pringles, respectively. The apparent differences in thickness and curvature between designs are intentional and are used to tune the ratio q/q_c (see Table I). **(d,e,f)** Experimental profile $z(x,y)$ of the liquid surface around the above objects in a color scale, as measured by a Schlieren method [46, 47] **(g)** Fitted profile of the interface for one central negative monopole q_c represented by the blue dot **(h, i)** Fitted liquid interface for the linear combination of four discrete charges of magnitude q placed inside the objects and a central negative monopole q_c, following Eq. (6).

TABLE I. Geometrical and capillary properties of the three types of 3D-printed multipolar objects.

	Eccentricity e	a [mm]	Thickness [mm]	q/q_c
Flat disk	0	5	0.4	0
Curved ellipse	0.87	5	0.4	1.22
Versatile Pringles	0.55	2.5	0.6	0.24

the Bond number for our particles with thickness T, we found $Bo = \frac{(\rho_p - \rho_l)gaT}{\gamma} \sim 0.1 - 1$, meaning that the central monopolar component q_c should be taken into account.

The liquid interface deformation around a single floating particle is observed using an improved Schlieren method proposed by Metzmacher et al. [47], which is based on the work of Moisy et al. [46]. The experimental liquid profile around the particle is displayed in a color scale in Figure 4, where red represents positive elevation Δz and purple represents negative Δz. Around the objects, gradients become too strong, leading to some uncertainty regarding the liquid elevation. This zone is, therefore, not measured and corresponds to the white zone around objects on profilometry pictures.

In profilometry pictures, one can directly notice the difference between a flat monopolar object and a curved quadrupolar object. For the quadrupolar objects, positive and negative charges q accounting for the four lobes were considered in addition to the negative central monopole q_c. We approximated the experimental profile well using a linear combination of those charges. The fitted profiles around our multipolar objects are shown in Figure 4(g,h,i).

IV. EXPERIMENTS

To validate our model, experiments were conducted using the 3D-printed multipolar objects presented in the previous section. Two identical objects were positioned at a distance $r_0 \gg a$ on a flat water–air interface using tweezers, the most reliable method

we found to minimize disturbances. This method can occasionally impart a slight initial velocity to the particles and results in a small variability in r_0 (15–30 mm). While this affects the time to contact, it does not change the nature of the capillary interaction. In fact, the residual motion from manual placement is quickly damped by viscosity, after which the capillary interaction dominates and drives the reorientation and attraction, thereby highlighting the robustness of the experiments to the initial conditions. Reorientation and attraction between the floating objects were observed, and their trajectories and orientations were recorded. The interdistance $r(t)$ and the objects' orientations over time $\theta_1(t)$ and $\theta_2(t)$ were then extracted from the sequence of images.

Experimental data of the spacing and the orientation over time of a pair of curved ellipses from one typical experiment are shown in Figure 5. We observe that the spacing $r(t)$ follows a logarithmic-like decay because, given the size of our objects, the $K_1(r/\lambda)$ behaves like an exponential decay. This is observed for all object types, whether quadrupolar or not. However, the decay rate varies significantly with the quadrupolar components and the initial orientations. Looking at the orientations, we observe a reorientation over time that leads to a final favored configuration, the end-to-end orientation in the present case. No particular orientation is observed between non-curved disks. In order to give a better view of the orientation process, more experimental evolutions of configuration (θ_1, θ_2) between pairs of curved ellipses and versatile Pringles are shown in colors in Figure 3(a) and (b), respectively. The gray-scale background represents the contour plot diagram corresponding to the opposite of the orientational term $-\Phi(\theta_1, \theta_2)$ in the interaction potential. Figure 3(a) shows that curved ellipses reorient themselves in the end-to-end configuration. This effect has been observed in all experiments with curved ellipses. One can also see that corotation is observed since the evolution of the orientations follows the diagonals $|\theta_1| = |\theta_2|$ and $|\theta_1| = |\pi - \theta_2|$ of the diagram of Figure 3. This corotation has been reported by Stamou et al. for circular quadrupolar particles [37].

Figure 3(b) shows orientations between versatile Pringles, our specially designed objects that follow the condition of Eq. (11), and whose positive charges are on the major axis. As predicted by the energy landscape, these objects can reorient themselves in the side-by-side configuration $\{\frac{\pi}{2}, \frac{\pi}{2}\}$. However, if we flip them, as the negative charges will now be on the major axis, the preferred orientation will therefore be end-to-end. The same objects can achieve two completely different configurations, which explains our choice to call them *versatile* Pringles. This versatility is shown in Figure 1(b-c) where an end-to-end configuration is observed for versatile Pringles with negative charges along the major axis (b) while flipping the particles results in a side-by-side configuration (c).

To further characterize the dynamics and reveal the importance of both the initial orientations and the quadrupolar component through the ratio q/q_c in the self-assembly process, we can numerically solve the equations of motion given in Eq. (12). The numerical solutions are presented for the initial condition of the experimental data shown in Figure 5, and we observe good agreement between the model and the experiments. The equations were numerically integrated using the Runge-Kutta method

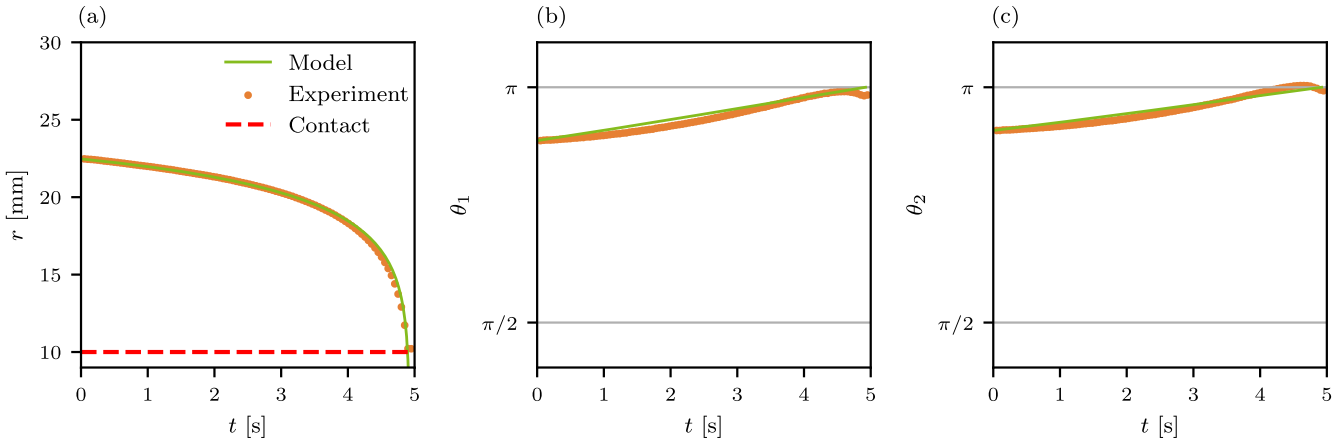

FIG. 5. Typical evolutions of **(a)** spacing $r(t)$ and orientations **(b)** $\theta_1(t)$ and **(c)** $\theta_2(t)$ between two curved ellipses before contact. Orange dots represent the experimental data, and green curves represent the numerical solutions of the coupled equations of motion given in Eq. (12). The red dotted line represents the distance at contact.

of order 5(4), also known as the Dormand-Prince method, which is implemented in the solve_ivp function from the SciPy library in Python. Resistance coefficients c and c' were calibrated on multiple experiments for each type of particle to fit their experimental attraction and reorientation rate. For each quadrupolar type of particle, both the experiments and the equations of motion reveal the coupling between the orientation and the attraction for these quadrupolar objects.

With the resistance coefficients calibrated on our experimental data for both the curved ellipse and the versatile Pringles type of objects, we were able to numerically acquire the dynamics of the self-assembly and the reorientation for all sets of initial interdistance r_0 and orientations $\{\theta_{1,0}, \theta_{2,0}\}$. Additionally, we can numerically compare the quadrupolar effect, which we call the "Pringles effect" and the monopolar-only effect, the Cheerios effect. Figure 6(a) and (b) illustrate, for curved ellipse and

versatile Pringles respectively, the time ratio $\tau = t/t_{cc}$ between the attraction time until contact for two quadrupolar objects t and the attraction time for the same uncurved ($q = 0$) objects t_{cc} from an initial distance $r_0 = 25$ mm for orientation $\theta_{1,0}$ and $\theta_{2,0}$ ranging from 0 to π. Red and purple regions indicate that the system reaches an end-to-end or side-by-side state, respectively. Hatched regions represent initial orientations for which contact was not reached after 10000 seconds of simulation. The versatile Pringles exhibit a stronger preference for side-by-side assembly over a broader range of initial orientations than the curved ellipses, a trend amplified by short-range interactions that are not taken into account in the present study. Differences between the curved ellipse and the versatile Pringles can also be seen in the time ratio τ. Indeed, while the quadrupolar component of the curved ellipse strongly strengthens the attraction whenever attraction is possible, it weakens the far-range attraction for the versatile Pringles except inside the green contours, representing a time ratio τ equal to 1. Figure 6 allows a straightforward comparison between the Pringles and the Cheerios Effect, highlighting the impact of the quadrupolar components on the self-assembly time and pattern.

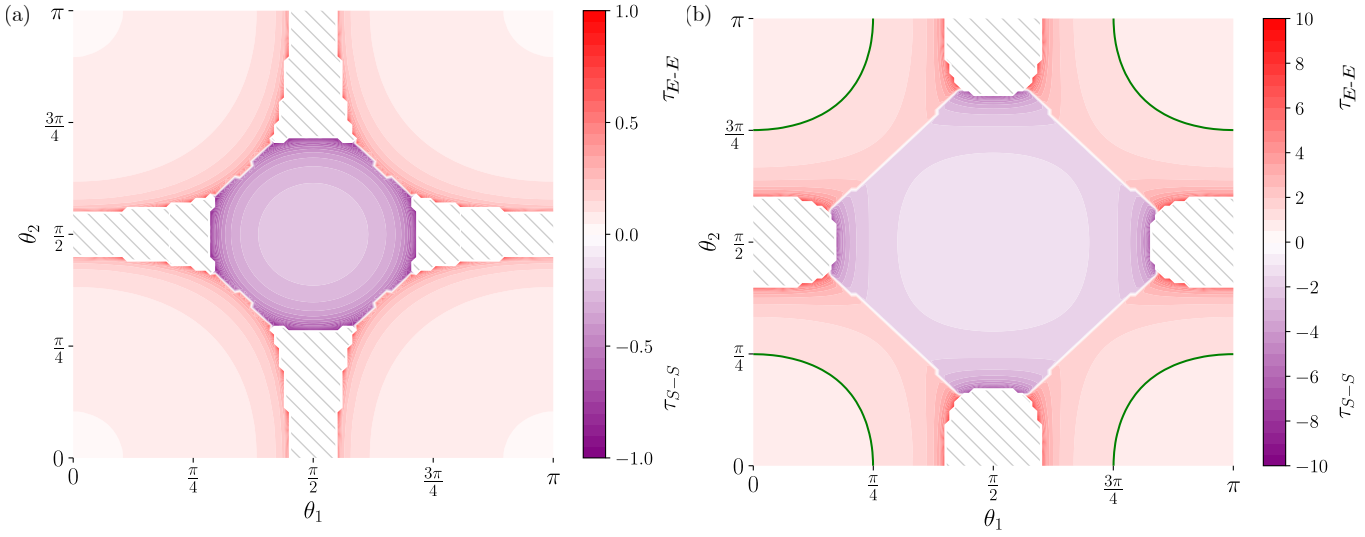

FIG. 6. Time ratio $\tau = t/t_{cc}$ between the attraction time t for quadrupolar objects and the attraction time t_{cc} for their uncurved counterparts ($q = 0$) as a function of their initial orientations. Contour plots depict the normalized attraction time τ for (a) curved ellipses and (b) versatile Pringles. The initial interdistance is fixed at $r_0 = 25$ mm, with initial orientations $\theta_{1,0}$ and $\theta_{2,0}$ varying from 0 to π. Red and purple regions indicate final end-to-end (τ_{E-E}) and side-by-side (τ_{S-S}) configurations, respectively, while hatched regions correspond to cases where contact was not reached within 10000 s. Green contours mark $\tau = 1$, where the attraction time equals that of uncurved objects.

While our theoretical study focuses on long- and near-field interactions between two bodies, Figure 1(d-e) reveals that by tailoring the quadrupolar and anisotropic properties of floating objects, we can also select final configurations between multiple bodies. When three or more particles are introduced to the interface, new configurations—metastable or stable—arise. For versatile Pringles with negative charges on the major axis, end-to-end chaining occurs as well as a "flower-like" structure where the tips of the ellipses touch in the center of a triangle, as one can observe in Figure 1(d). These contact configurations have been observed in different studies with objects possessing similar quadrupolar shapes of the meniscus and can be attributed to multibody effects [16, 17, 24, 35, 48]. One can easily understand that these configurations are favored because the central negative charge reinforces the negative tips of the ellipses. When we flip the particles, the negative charges are now on the minor axis, and we observe side-by-side chaining as well as a triangular structure where the ellipse tips touch at the corners of an equilateral triangle in Figure 1(e). Again, it is straightforward that these configurations are the way to make the sides of the ellipses closer. Although such assemblies, particularly the end-to-end chains, can be metastable, capillary bridges may appear due to the shape of the particles and stabilize the chains [25, 49]. We note that these multi-particle configurations were observed qualitatively and are included here for illustration; a systematic study of their stability and assembly pathways lies beyond the scope of the present work and will be the subject of future investigations.

V. CONCLUSION

Our comprehensive study confirms that the design and orientation of anisotropic quadrupolar objects significantly influence their self-assembly behavior on a liquid-air interface. The versatile Pringles, tailored with specific geometrical and capillary properties, successfully demonstrated the predicted end-to-end and side-by-side configurations under experimental conditions.

The theoretical models aligned closely with empirical observations, highlighting the role of the Pringles effect in guiding the self-assembly process. This effect, coupled with the ability to toggle between configurations by simply flipping the objects, opens new avenues for constructing complex, reprogrammable structures.
Future work will focus on refining the design parameters and exploring the stability of assembled structures, potentially extending the application of this technology to areas such as programmable materials and adaptive manufacturing.

AUTHOR CONTRIBUTIONS

Both authors have developed the original idea and elaborated the theoretical models. MD has modeled and 3D-printed the particles, performed all experiments and data analysis, and wrote the article. Both authors have participated in the editing of the manuscript.

CONFLICTS OF INTEREST

There are no conflicts to declare.

DATA AVAILABILITY

Data for this article, including experimental data presented in Figures 3, 4 and 5, zoomed-in pictures to evaluate the objects' surface roughness and STL files for all 3D-printed objects presented here, are available at Zenodo at `https://doi.org/10.5281/zenodo.11282790`[45].

ACKNOWLEDGEMENTS

This work is financially supported by the University of Liège through the CESAM Research Unit and the FNRS CDR project number J.0186.23 entitled "Magnetocapillary Interactions for Locomotion at Liquid Interfaces" (MILLI).

APPENDIX: CALCULATION OF THE POTENTIAL

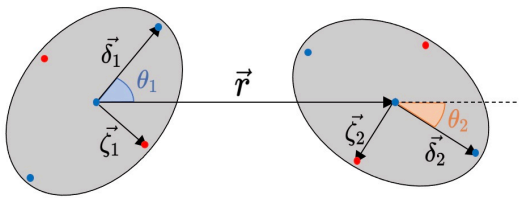

FIG. 7. Schematics of two elliptic quadrupolar objects at distance r. Vectors $\vec{\delta}$ and $\vec{\zeta}$ and angles θ_1 and θ_2 that describe their relative positions and orientations are indicated.

Following the sketch of Figures 2 and 7, one has to consider 16 terms for calculating the interaction potential between two

quadrupoles U_{qq}. One has

$$\begin{aligned} U_{qq} = &-2\pi\gamma q^2 \sum_{\text{pairs}} K_0\left(\frac{\left|\vec{r}\pm\vec{\delta}_1\pm\vec{\delta}_2\right|}{\lambda}\right) \\ &-2\pi\gamma q^2 \sum_{\text{pairs}} K_0\left(\frac{\left|\vec{r}\pm\vec{\zeta}_1\pm\vec{\zeta}_2\right|}{\lambda}\right) \\ &+2\pi\gamma q^2 \sum_{\text{pairs}} K_0\left(\frac{\left|\vec{r}\pm\vec{\delta}_1\pm\vec{\zeta}_2\right|}{\lambda}\right) \\ &+2\pi\gamma q^2 \sum_{\text{pairs}} K_0\left(\frac{\left|\vec{r}\pm\vec{\zeta}_1\pm\vec{\delta}_2\right|}{\lambda}\right) \end{aligned} \tag{13}$$

where the first two sums correspond to the eight attractive interactions between two vertices of the same charge, and the last terms correspond to the repulsive interactions between opposite charges. One should remark that each Bessel function in the previous equation is of the form

$$K_0\left(\frac{|\vec{r}\pm\vec{\zeta}_1\pm\vec{\zeta}_2|}{\lambda}\right) = K_0\left(\frac{r}{\lambda}\sqrt{1+2\alpha x+2\beta x^2}\right) \tag{14}$$

where the reduced variable $x = a/r$ is small when the objects are far from each other. The remaining parameters α and β differ for each term and depend on the object's size and orientation. The leading orders of the Taylor expansion of Eq. (14) when $r \gg a$ gives

$$\begin{aligned} K_0\left(\frac{r}{\lambda}\sqrt{1+2\alpha x+2\beta x^2}\right) \overset{(r\gg a)}{\approx} & K_0\left(\frac{r}{\lambda}\right) - \frac{\alpha r x}{\lambda}K_1\left(\frac{r}{\lambda}\right) + \frac{rx^2}{2\lambda^2}\left[2\lambda\left(\alpha^2-\beta\right)K_1\left(\frac{r}{\lambda}\right) + \alpha^2 r K_0\left(\frac{r}{\lambda}\right)\right] \\ &- \frac{x^3\alpha r}{6\lambda^3}\left[K_1\left(\frac{r}{\lambda}\right)\left(4\lambda^2\left(2\alpha^2-3\beta\right)+\alpha^2r^2\right) + 2\lambda r\left(2\alpha^2-3\beta\right)K_0\left(\frac{r}{\lambda}\right)\right] \\ &+ \frac{rx^4}{24\lambda^4}\left[rK_0\left(\frac{r}{\lambda}\right)\left(12\lambda^2\left(2\alpha^4-4\alpha^2\beta+\beta^2\right)+\alpha^4r^2\right)\right. \\ &\qquad \left. + 4\lambda K_1\left(\frac{r}{\lambda}\right)\left(6\lambda^2\left(2\alpha^4-4\alpha^2\beta+\beta^2\right)+r^2\left(2\alpha^4-3\alpha^2\beta\right)\right)\right] \\ &+ O\left(x^5\right) \end{aligned} \tag{15}$$

Considering these terms in Eq. (13), the zero-order term becomes null since the sum of all capillary charges is zero. The first three orders are also zero from symmetry arguments because the sum of the four α's and α^2's is zero. One has to reach the fourth order to obtain a non-zero term in the series. The fourth non-vanishing term $\sim r^4x^4$ in this Taylor expansion is given by

$$\frac{1}{24}\alpha^4\left(\frac{r}{\lambda}\right)^4 K_0\left(\frac{r}{\lambda}\right)x^4 \tag{16}$$

The sum of all different α^4 's gives the orientational term

$$\Gamma(\theta_1,\theta_2) = -6\left(\left(a^2+b^2\right)\cos(2\theta_1)+a^2-b^2\right)\times\left(\left(a^2+b^2\right)\cos(2\theta_2)+a^2-b^2\right) \tag{17}$$

The interaction potential between one quadrupole and one central monopole U_{cq} has been calculated with the same approach.

[1] N. Bowden, A. Terfort, J. Carbeck, and G. M. Whitesides, Self-assembly of mesoscale objects into ordered two-dimensional arrays, Science **276**, 233 (1997).

[2] S. E. Chung, W. Park, S. Shin, S. A. Lee, and S. Kwon, Guided and fluidic self-assembly of microstructures using railed microfluidic channels, Nature materials **7**, 581 (2008).

[3] M. Boncheva and G. M. Whitesides, Making things by self-assembly, MRS bulletin **30**, 736 (2005).

[4] L. Zhang, J. M. Chan, F. X. Gu, J.-W. Rhee, A. Z. Wang, A. F. Radovic-Moreno, F. Alexis, R. Langer, and O. C. Farokhzad, Self-assembled lipid- polymer hybrid nanoparticles: a robust drug delivery platform, ACS nano **2**, 1696 (2008).

[5] S.-H. Kim, S. Y. Lee, S.-M. Yang, and G.-R. Yi, Self-assembled colloidal structures for photonics, NPG Asia Materials **3**, 25 (2011).

[6] Y. Xia, B. Gates, and Z.-Y. Li, Self-assembly approaches to three-dimensional photonic crystals, Advanced Materials **13**, 409 (2001).

[7] B. A. Grzybowski, H. A. Stone, and G. M. Whitesides, Dynamic self-assembly of magnetized, millimetre-sized objects rotating at a liquid–air interface, Nature **405**, 1033 (2000).

[8] G. M. Whitesides and B. Grzybowski, Self-assembly at all scales, Science **295**, 2418 (2002).

[9] J. A. Pelesko, *Self assembly: the science of things that put themselves together* (Chapman and Hall/CRC, 2007).

[10] M. M. Nicolson, The interaction between floating particles, Math. Proc. Cambridge Philos. Soc. **45**, 288 (1949).

[11] D. Chan, J. Henry Jr, and L. White, The interaction of colloidal particles collected at fluid interfaces, J. Colloid Interface Sci. **79**, 410 (1981).

[12] D. Vella and L. Mahadevan, The "Cheerios effect", Am. J. Phys. **73**, 817 (2005).

[13] M.-J. Dalbe, D. Cosic, M. Berhanu, and A. Kudrolli, Aggregation of frictional particles due to capillary attraction, Physical Review E **83**, 051403 (2011).

[14] K. D. Danov and P. A. Kralchevsky, Capillary forces between particles at a liquid interface: General theoretical approach and interactions between capillary multipoles, Advances in colloid and interface science **154**, 91 (2010).

[15] K. Hosokawa, I. Shimoyama, and H. Miura, Two-dimensional micro-self-assembly using the surface tension of water, Sensors and Actuators A: Physical **57**, 117 (1996).

[16] J. Loudet and B. Pouligny, How do mosquito eggs self-assemble on the water surface?, The European Physical Journal E **34**, 1 (2011).

[17] J. Voise, M. Schindler, J. Casas, and E. Raphaël, Capillary-based static self-assembly in higher organisms, Journal of The Royal Society Interface **8**, 1357 (2011).

[18] P. W. Rothemund, Using lateral capillary forces to compute by self-assembly, Proceedings of the National Academy of Sciences **97**, 984 (2000).

[19] M. Poty, G. Lumay, and N. Vandewalle, Customizing mesoscale self-assembly with three-dimensional printing, New Journal of Physics **16**, 023013 (2014).

[20] J. Metzmacher, M. Poty, G. Lumay, and N. Vandewalle, Self-assembly of smart mesoscopic objects, The European Physical Journal E **40**, 1 (2017).

[21] N. Vandewalle, L. Clermont, D. Terwagne, S. Dorbolo, E. Mersch, and G. Lumay, Symmetry breaking in a few-body system with magnetocapillary interactions, Physical Review E **85**, 041402 (2012).

[22] J.-C. Loudet, A. M. Alsayed, J. Zhang, and A. G. Yodh, Capillary interactions between anisotropic colloidal particles, Physical review letters **94**, 018301 (2005).

[23] H. Lehle, E. Noruzifar, and M. Oettel, Ellipsoidal particles at fluid interfaces, The European Physical Journal E **26**, 151 (2008).

[24] B. Madivala, J. Fransaer, and J. Vermant, Self-assembly and rheology of ellipsoidal particles at interfaces, Langmuir **25**, 2718 (2009).

[25] E. P. Lewandowski, M. Cavallaro Jr, L. Botto, J. C. Bernate, V. Garbin, and K. J. Stebe, Orientation and self-assembly of cylindrical particles by anisotropic capillary interactions, Langmuir **26**, 15142 (2010).

[26] E. P. Lewandowski, J. A. Bernate, P. C. Searson, and K. J. Stebe, Rotation and alignment of anisotropic particles on nonplanar interfaces, Langmuir **24**, 9302 (2008), pMID: 18661958, https://doi.org/10.1021/la801167h.

[27] D. Ershov, J. Sprakel, J. Appel, M. A. Cohen Stuart, and J. van der Gucht, Capillarity-induced ordering of spherical colloids on an interface with anisotropic curvature, Proceedings of the National Academy of Sciences **110**, 9220 (2013).

[28] J. Eatson, S. Bauernfeind, B. Midtvedt, A. Ciarlo, J. Menath, G. Pesce, A. B. Schofield, G. Volpe, P. S. Clegg, N. Vogel, D. M. A. Buzza, and M. Rey, Self-assembly of defined core–shell ellipsoidal particles at liquid interfaces, Journal of Colloid and Interface Science **683**, 435 (2025).

[29] N. Hazra, A. A. Rudov, J. Midya, A. Babenyshev, S. Bochenek, M. Frenken, W. Richtering, G. Gompper, T. Auth, I. I. Potemkin, *et al.*, Capillary-driven self-assembly of soft ellipsoidal microgels at the air–water interface, Proceedings of the National Academy of Sciences **121**, e2403690121 (2024).

[30] P.-G. Gennes, F. Brochard-Wyart, D. Quéré, *et al.*, *Capillarity and wetting phenomena: drops, bubbles, pearls, waves* (Springer, 2004).

[31] K. D. Danov, P. A. Kralchevsky, B. N. Naydenov, and G. Brenn, Interactions between particles with an undulated contact line at a fluid interface: Capillary multipoles of arbitrary order, Journal of colloid and interface science **287**, 121 (2005).

[32] Á. Domínguez Álvarez, M. Oettel, and S. Dietrich, Force balance of particles trapped at fluid interfaces, The Journal of Chemical Physics, 128 (11), 10.1063. (2008).

[33] P. A. Kralchevsky and K. Nagayama, Capillary forces between colloidal particles, Langmuir **10**, 23 (1994).

[34] P. A. Kralchevsky, N. D. Denkov, and K. D. Danov, Particles with an undulated contact line at a fluid interface: interaction between capillary quadrupoles and rheology of particulate monolayers, Langmuir **17**, 7694 (2001).

[35] A. Brown, C. Smith, and A. Rennie, Fabricating colloidal particles with photolithography and their interactions at an air-water interface, Physical Review E **62**, 951 (2000).

[36] L. Botto, E. P. Lewandowski, M. Cavallaro, and K. J. Stebe, Capillary interactions between anisotropic particles, Soft Matter **8**, 9957 (2012).

[37] D. Stamou, C. Duschl, and D. Johannsmann, Long-range attraction between colloidal spheres at the air-water interface: The consequence of an irregular meniscus, Physical Review E **62**, 5263 (2000).

[38] J. Metzmacher, M. Delens, and N. Vandewalle, Ring of capillary actuators as trap, tweezers, and ratchet for floating particles (2024), preprint (Version 1) available at Research Square.

[39] P. A. Kralchevsky and N. D. Denkov, Capillary forces and structuring in layers of colloid particles, Current opinion in colloid & interface science **6**, 383 (2001).

[40] P. A. Kralchevsky and K. Nagayama, Capillary interactions between particles bound to interfaces, liquid films and biomembranes, Ad-

vances in colloid and interface science **85**, 145 (2000).
[41] N. D. Vassileva, D. van den Ende, F. Mugele, and J. Mellema, Capillary forces between spherical particles floating at a liquid- liquid interface, Langmuir **21**, 11190 (2005).
[42] M. Delens, Y. Collard, and N. Vandewalle, Induced capillary dipoles in floating particle assemblies, Physical Review Fluids **8**, 074001 (2023).
[43] M. Delens, A. Franckart, D. M. Harris, and N. Vandewalle, 3d-printed spines for programmable liquid topographies and micromanipulation, Nature Communications **16**, 1 (2025).
[44] N. Vandewalle, M. Poty, N. Vanesse, J. Caprasse, T. Defize, and C. Jérôme, Switchable self-assembled capillary structures, Soft Matter **16**, 10320 (2020).
[45] M. Delens and N. Vandewalle, Data and stl files supporting article: Encoding quadrupolar capillary information into saddle- shaped objects for self-assembly, 10.5281/zenodo.11282790 (2024).
[46] F. Moisy, M. Rabaud, and K. Salsac, A synthetic schlieren method for the measurement of the topography of a liquid interface, Experiments in Fluids **46**, 1021 (2009).
[47] J. Metzmacher, G. Lagubeau, M. Poty, and N. Vandewalle, Double pattern improves the schlieren methods for measuring liquid–air interface topography, Experiments in Fluids **63**, 120 (2022).
[48] Z. Zhang, P. Pfleiderer, A. B. Schofield, C. Clasen, and J. Vermant, Synthesis and directed self-assembly of patterned anisometric polymeric particles, Journal of the American Chemical Society **133**, 392 (2011).
[49] L. Botto, L. Yao, R. Leheny, and K. Stebe, Capillary bond between rod-like particles and the micromechanics of particle-laden interfaces, Soft Matter **8**, 4971 (2012).